

## FE Analysis of a Notched Cylinder under Multiaxial Cyclic Loading Using the Multilayer Model of Besseling

G. Savaidis<sup>1</sup>, N. Pitzis<sup>1</sup>, A. Savaidis<sup>1</sup> and Ch. Zhang<sup>2</sup>

**Abstract:** This paper presents an elastic-plastic finite element analysis of a circumferentially notched cylinder subjected to multiaxial non-proportional fatigue loading. Two different load combinations are investigated: (1) constant tension with cyclic torsion and (2) constant torsion with cyclic tension. The multilayer plasticity model of Besseling in conjunction with the von Mises yield criterion is applied to describe the elastic-plastic material behaviour. The parametrical study contains a coarse and a fine finite element mesh with and without mid-nodes as well as three different types of multilinear approximations of the material law, namely, a twenty-segments, a five-segments and a three-segments one. The comparison between the present numerical results and those from previous works obtained from Prager-Ziegler's bilinear material model shows an improved accuracy of the numerical modelling. By using the numerical results, the basic relations between the applied loads and the local stress-strain responses at the notch-root are analyzed.

**Keywords:** Notched cylinder, Multiaxial fatigue; Finite element method, Elastic-plastic analysis, Multilayer plasticity model.

### 1 Introduction

Geometrical discontinuities, such as notches exist in many engineering components and structures due to special functional and design requirements. These geometrical irregularities may cause significant stress concentrations at the notch-root. Such stress concentrations often result in the development of intense plastic deformations at the

notch-root, and hence induce an early crack initiation under service loading conditions. At the notch-root of an engineering component, a multiaxial stress-strain state exists in general even if the component is subjected to a uniaxial cyclic loading. A realistic and reliable fatigue-life prediction model should take both the stress-strain concentrations and the local multiaxiality at the notch-root into account.

To develop a life prediction model, the basic local stress-strain relations and the damage evolution process at the notch-root should be well understood. In previous works of Savaidis, Savaidis and Zhang (2001) and Savaidis, Savaidis and Zhang (2002) some basic investigations using the kinematic hardening rule of Prager (1955) and Ziegler (1959) in conjunction with the von Mises yield criterion, see von Mises (1913), have been performed. The Prager-Ziegler's kinematic hardening rule is capable to describe linear material hardening in a reliable way. Due to its simplicity, it is implemented in many commercial finite element programs. However, neither the material cyclic stress-strain curve nor the hysteresis loops can be described adequately by a linear hardening rule, see Lemaitre and Chaboche (1990). In this case, the stress-strain responses under fatigue loading may not be accurately modeled, which could lead consequently to unreliable material damage estimations. Such situations may occur for instance in low-cycle fatigue where high plastic strains are introduced, or in fatigue loading with variable amplitudes where a linear kinematic hardening model is not capable to provide a realistic transposition of the yield surface within the whole stress spectrum.

To overcome the abovementioned drawbacks, several improvements have been proposed during

---

<sup>1</sup> Aristotle University Thessaloniki, Greece

<sup>2</sup> University of Siegen, Germany

the last decades. Some of the improved models aimed at providing a satisfactory representation of the stress-strain material responses on smooth specimens, see e.g. Hassan and Kiriakides (1994), while others incorporated the presence of structural discontinuities such as notches to the stress-strain responses in the critical region of the structures, see e.g. Hoffmann and Seeger (1985) and Köttgen and Seeger (1993). For a better approximation of the nonlinear stress-strain responses, several multisurface models or multilayer (overlay) models have been proposed in literature, e.g. Mroz (1967), Besseling (1958), Iwan (1966), Iwan (1967), Owen, Prakash and Zienkiewicz (1974), Pande, Owen and Zienkiewicz (1977), Chiang and Beck (1994), Schiffner (1995) and Yoon, Hong and Lee (2004). Logically, a nonlinear stress-strain curve can be approximated more accurately by means of multi-segments instead of only two segments.

Within the framework of the finite element method, a material model describing accurately cyclic plasticity is indispensable. However, a universal material model has yet not been provided for commercial FE codes. In this context, we just mention the recent significant work of Hertel, Döring, Hoffmeyer, Seeger and Vormwald (2005), who implemented the superior plasticity model of Döring, Hoffmeyer, Seeger and Vormwald (2003) for computing the stress-strain responses under multiaxial non-proportional fatigue loading into the commercial FE package ABAQUS.

With this motivation in mind, the present work takes a further step to the previous investigations of Savaidis, Savaidis and Zhang (2001) and Savaidis, Savaidis and Zhang (2002) by incorporating an advanced and more efficient multilayer plasticity model into the multiaxial fatigue analysis of the notched cylinder problem. Special attention of the present analysis is devoted to achieve a better understanding of the local mechanical responses at the notch-root under multiaxial non-proportional fatigue loading, and to obtain quantitatively reliable numerical results.

With the abovementioned aims, a parametrical study on a notched axisymmetric circular cylin-

der subjected to multiaxial non-proportional synchronous cyclic loading is performed by means of an elastic-plastic finite element method. The multilinear or overlay plasticity model of Besseling and the von Mises yield criterion are applied to describe the elastic-plastic material properties. Two different loading combinations are investigated: a) constant tension-compression combined with cyclic torsion, and b) constant torsion superposed by cyclic tension-compression. Numerical results for normal stress-normal strain and shear stress-shear strain curves at the notch-root are presented and discussed. The influences of the finite element mesh quality, i.e. the types and the size of the elements used especially in the critical region (notch-root), on the numerical results are investigated. Furthermore, the effects of the segment number to approximate the material's stress-strain curve on the numerical results are analyzed and discussed.

It should be noted here that the present work does not incorporate comparisons with experimental results, since such test results for the investigated shaft-notch geometry, material parameters and loading combinations cannot be found in literature. Until now, only very few experimental results for the stress-strain responses at mild notch roots were reported in literature due to the fact that it is very difficult to access the root of a sharp notch and it requires quite complex test devices for multiaxial nonproportional fatigue measurements. As a future research subject, the authors will conduct experimental verifications by comparing the present FE results and the measured experimental data, which will be determined from notched specimens as investigated in the present work.

## 2 Problem formulation and governing equations

Let us consider an infinitely long and elastic-plastic cylinder with a circumferential notch as shown in Fig. 1.

The geometrical parameters of the cylinder under investigation are summarized in Tab. 1.

A tensile force  $N$  and a torsional moment  $M_T$  are

Table 1: Geometrical parameters of the notched shaft

Shaft diameter $D$ (mm)	Crucial diameter $D_i$ (mm)	Notch depth $t$ (mm)	Notch radius $\rho$ (mm)
140	70	35	3

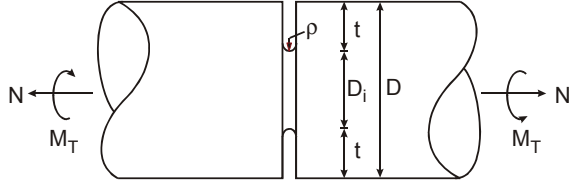


Figure 1: The infinite notched shaft

applied to the notched cylinder. For convenience, the nominal tensile stress  $S$  and the nominal shear stress  $T$ , instead of  $N$  and  $M_T$  are used as external loads in the analysis, which are related by

$$S = \frac{N}{\pi(D_i/2)^2}, \quad T = \frac{2M_T}{\pi(D_i/2)^3} \quad (1)$$

where  $D_i$  is the inner diameter of the notched shaft. In general, the loading components  $S$  and  $T$  are time dependent and can be written as

$$S(t) = S_m \pm S_a \cdot f(t), \quad T(t) = T_m \pm T_a \cdot g(t), \quad (2)$$

where  $f(t)$  and  $g(t)$  are the normalized time functions,  $S_m$  and  $T_m$  are the mean values, while  $S_a$  and  $T_a$  are the amplitudes of the tensile and the torsional loading components, respectively. The loading components are regarded as synchronous and non-proportional, when

$$f(t) = g(t), \quad S(t)/T(t) \neq \text{const}. \quad (3)$$

Equation (3) implies that both loading components should have the same phase and frequency, while their mean values and/or amplitudes may take different values. It should be noted here that the important loading case to engineering applications of superposing a constant loading with a variable cyclic loading component belongs to the synchronous non-proportional loading combination.

In the present analysis a parametrical study of several loading combinations is carried out. In the

first group of loading cases, static tensile loading components are combined with cyclic torsional ones. In the second loading group, various loading cases with static torsional loading components superposed by cyclic tensile loading components are considered.

The notched cylinder satisfies the equilibrium equations

$$\sigma_{ij,j} + f_i = 0, \quad (4)$$

where  $\sigma_{ij}$  denotes the stress components,  $f_i$  the body-force components, and a comma represents partial derivatives with respect to  $x_j$ . It is assumed in the analysis that the deformation is small, i.e., the strain components  $\varepsilon_{ij}$  are related to the displacement components  $u_i$  by the following linear kinematic relation

$$\varepsilon_{ij} = \frac{1}{2}(u_{i,j} + u_{j,i}). \quad (5)$$

The elastic-plastic material properties of the notched cylinder are described by the multilayer or overlay plasticity model of Besseling. According to the multilayer plasticity model, the material is assumed to be consisting of various overlays or subelements. All the subelements are subjected to the same total strain, but each subelement has different yield strength. Each subelement exhibits an elastic-perfectly plastic material behavior. Although a simple stress-strain behavior is assumed for each subelement, the multilayer model is able to properly describe quite complex elastic-plastic material behaviors such as the Bauschinger effect or the kinematic hardening. In the multilayer model, each subelement has the same strain pattern but different stress field  $(\sigma_{ij})_n$ . The overall stresses are the weighted sum of the stresses in the subelements

$$\sigma_{ij} = \sum_{n=1}^N w_n \cdot (\sigma_{ij})_n, \quad (6)$$

where the weighting factor satisfies

$$\sum_{n=1}^N w_n = 1, \quad w_n = \frac{E - E_{Tn}}{E - \frac{1-2\nu}{3}E_{Tn}} - \sum_i^{n-1} w_i. \quad (7)$$

In Eqs. (6) and (7),  $w_n$  is the weighting factor of the  $n$ -th subelement,  $N$  is the number of the subelements, and  $E_{Tn}$  is the slope of the  $n$ -th segment of the uniaxial stress-strain curve of the material.

According to ANSYS (2007), the yield stress for each subelement is determined by

$$(\sigma_y)_n = \frac{1}{2(1+\nu)} [3E\varepsilon_n - (1-2\nu)\sigma_n], \quad (8)$$

where  $(\varepsilon_n, \sigma_n)$  is the  $n$ -th vertex of the multi-linear uniaxial stress-strain curve. The total number of subelements is equal to the number of vertexes specified.

The von Mises yield criterion for each subelement takes the following form

$$F = J_2'(\sigma_{ij}) - \sigma_y = 0, \quad (9)$$

where the subscript  $n$  for the  $n$ -th subelement is omitted here and in what follows for the sake of brevity. In Eq. (9),  $J_2'(\sigma_{ij})$  is the second invariant of the stress deviator

$$J_2'(\sigma_{ij}) = \frac{1}{2} \sigma_{ij}' \cdot \sigma_{ij}', \quad (10)$$

where  $\sigma_{ij}'$  is the stress deviator

$$\sigma_{ij}' = \sigma_{ij} - \frac{1}{3} \sigma_{kk} \delta_{ij}, \quad (11)$$

and  $\delta_{ij}$  denotes the Kronecker symbol.

The consistency condition during plastic loading is given by

$$dF = \frac{\partial F}{\partial \sigma_{ij}} \cdot d\sigma_{ij} = 0. \quad (12)$$

The total strain increment is written as a sum of an elastic part and a plastic part

$$d\varepsilon_{ij} = d\varepsilon_{ij}^e + d\varepsilon_{ij}^p. \quad (13)$$

The elastic strain increment is determined by Hooke's law

$$d\sigma_{ij} = E_{ijkl} d\varepsilon_{kl}^e, \quad (14)$$

where  $E_{ijkl}$  is the elasticity tensor. The plastic strain increment is determined by the flow or normality rule

$$d\varepsilon_{ij}^p = d\lambda \cdot \frac{\partial F}{\partial \sigma_{ij}}, \quad (15)$$

where  $d\lambda$  is the plastic multiplier. By using Eqs. (12)-(15) the plastic multiplier  $d\lambda$  can be obtained as

$$d\lambda = \frac{(\partial F / \partial \sigma_{ij}) \cdot E_{ijkl} \cdot d\varepsilon_{kl}}{(\partial F / \partial \sigma_{pq}) \cdot E_{pqrs} \cdot (\partial F / \partial \sigma_{rs})}. \quad (16)$$

Substitution of Eqs. (13), (15) and (16) into Eq. (14) results in the following incremental constitutive equations

$$d\sigma_{ij} = E_{ijkl}^* d\varepsilon_{kl}, \quad (17)$$

where the elastic-plastic tangent stiffness tensor  $E_{ijkl}^*$  is given by

$$E_{ijkl}^* = E_{ijkl} - \alpha \frac{M_{ij} M_{kl}}{M_{mn} \cdot (\partial F / \partial \sigma_{mn})}, \quad (18)$$

$$M_{ij} = E_{ijmn} \cdot \frac{\partial F}{\partial \sigma_{mn}}, \quad (19)$$

$$\alpha = \begin{cases} 0, & F < 0 \text{ or } F = 0 \text{ and } dF < 0, \\ 1, & F = 0 \text{ and } dF \geq 0. \end{cases} \quad (20)$$

The von Mises yield criterion with the associated flow rule as described afore is implemented in the commercial FEM-package ANSYS, which is applied in the present analysis to compute the plastic strain increment  $(\Delta\varepsilon_{ij}^p)_n$  for the  $n$ -th subelement. The overall plastic strain increments are the weighted sums of the plastic strain increments of the subelements

$$\Delta\varepsilon_{ij}^p = \sum_{n=1}^N w_n \cdot (\Delta\varepsilon_{ij}^p)_n, \quad (21)$$

where  $N$  is the total number of the subelements.

An Euler backward scheme is applied in the numerical implementation. The current plastic strain and the current elastic strain at the  $m$ -th iteration-step are updated by means of the following equations

$$(\varepsilon_{ij}^p)^m = (\varepsilon_{ij}^p)^{m-1} + \Delta\varepsilon_{ij}^p, \quad (22)$$

$$(\varepsilon_{ij}^e)^m = (\varepsilon_{ij}^{tr})^m - \Delta\varepsilon_{ij}^p, \quad (23)$$

where the trial strain  $(\varepsilon_{ij}^{tr})^m$  is defined as the total strain minus the plastic strain from the previous iteration-step

$$(\varepsilon_{ij}^{tr})^m = (\varepsilon_{ij})^m - (\varepsilon_{ij}^p)^{m-1}. \quad (24)$$

### 3 Finite element discretization

A Cartesian coordinate system is introduced in the analysis, where the Z-axis coincides with the symmetry axis of the cylinder. The X- and Y-axes are located on the plane of symmetry perpendicular to the Z-axis as shown in Fig. 2.

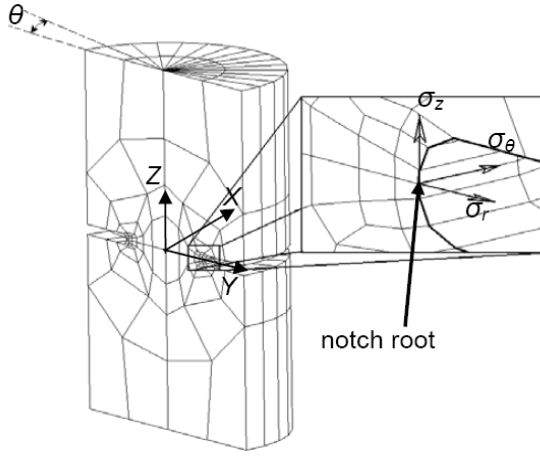


Figure 2: Finite element discretization and notch root mesh detail

In the pure linear elastic case for multiaxial tensile and torsional loading combination, an equivalent stress concentration factor  $K_{eq}$  is defined by Savaidis (2002) to describe the local stress concentration at the notch-root

$$K_{eq} = \sqrt{\frac{(1 - \bar{a}_e - \bar{a}_e^2)(K_t^S)^2 + 3(\frac{T}{S})^2(K_t^T)^2}{1 + 3(\frac{T}{S})^2}}, \quad (25)$$

or

$$K_{eq} = \frac{\sigma_{eq}}{S_{eq}}, \quad (26)$$

$$K_t^S = \frac{\sigma_Z}{S}, \quad K_t^T = \frac{\tau_{ZY}}{T}, \quad (27)$$

$$S_{eq} = \sqrt{S^2 + 3T^2}, \quad \bar{a}_e = \frac{\sigma_Y}{\sigma_Z}. \quad (28)$$

In Eqs. (25)-(28),  $K_{eq}$  represents the ratio between the local equivalent elastic stress  $\sigma_{eq}$  and the equivalent nominal stress  $S_{eq}$ . For the present geometry the stress concentration factors  $K_t^S = 3.69$  for pure tension and  $K_t^T = 2.01$  for pure torsion are obtained according to Peterson (1974).

In this paper, detailed finite element analyses are performed for two types of finite element discretization, both concerning the circumferentially notched shaft as shown in Fig. 1. Firstly, a coarse FE mesh with 1380 elements and 6077 nodes (consisting of thirty circular segments, each having an angle  $\theta=12^\circ$ , see detail (a) in Fig. 3) is applied. A finer FE discretization of the same geometry with 5760 elements and 23669 nodes is then used in the second investigation (see detail (b) in Fig. 3). The finer FE mesh consists of forty circular segments, each having an angle  $\theta=9^\circ$ . A section of the shaft on the XZ plane is shown in Fig. 3 for the coarse and the finer FE discretization. The accuracy of the numerical results and the required computing time are discussed in the following.

In the nonlinear FE analysis a full Newton-Raphson procedure according to Bathe (1996) for all degrees of freedom is applied. 3-D solid elements with 20-nodes and 14 Gaussian integration points are used in all numerical calculations presented here. Integration procedures at the Gaussian points and a subsequent extrapolation to the nodes of the investigated notch-elements have been applied for the evaluation of the local stress-strain responses at the notch-root.

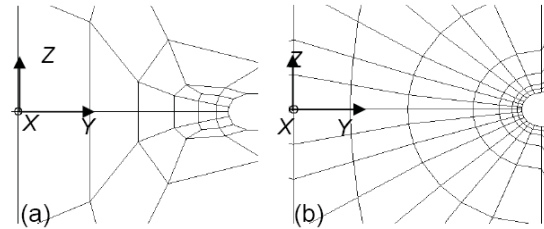


Figure 3: (a) Coarse and (b) fine finite element meshes

Aluminum alloy Al5083 is considered in all numerical investigations. Uniaxial low-cycle and high-cycle fully-reversed fatigue tests on smooth specimens have been performed by Savaidis (1995) to determine the cyclic stress-strain curve of the material. The fatigue tests were accomplished until visible small cracks with lengths of 0.5mm were initiated at the surfaces of the specimens, or at least a stabilized condition i.e., a practically unchanging stress value during the strain-controlled loading, was reached.

The cyclic hardening coefficient  $K'$  and the cyclic hardening exponent  $n'$  have been evaluated for the analytical description of the stabilized stress–strain curve according to the well-known material law of Ramberg and Osgood (1943)

$$\varepsilon_{\alpha} = \frac{\sigma_{\alpha}}{E} + \left( \frac{\sigma_{\alpha}}{K'} \right)^{\frac{1}{n'}}, \quad (29)$$

where  $\varepsilon_{\alpha}$  and  $\sigma_{\alpha}$  correspond to the amplitudes of the stabilized normal strain and normal stress values, respectively. The values of  $K'$  and  $n$  determined by means of statistical analyses of the experimental results are  $K'=544 \text{ N/mm}^2$  and  $n'=0.075$ . The experimentally determined elastic modulus  $E$  and Poisson's ratio  $\nu$  are given by  $E=68000 \text{ N/mm}^2$  and  $\nu=0.32$ , respectively.

#### 4 Loading cases

To examine the influences of the loading amplitude and the mean load on the local stress-strain behaviour at the notch-root, several multi-axial synchronous loading cases are investigated. They can be divided into two groups, which are described in the following.

##### 4.1 Loading group 1: Constant tension combined with cyclic torsion

Six combinations (loading cases L1 to L6) of constant tension and cyclic fully reversed torsion ( $R_{\tau} = T_{\min}/T_{\max} = -1$ ) with constant amplitudes are first investigated. Fig. 4 shows a schematic representation of the loading type, while Tab. 2 contains the values of the individual loading components.

For convenience, the ratio  $c = S_m/T_a$  of the constant nominal normal stress  $S_m$  to the nominal

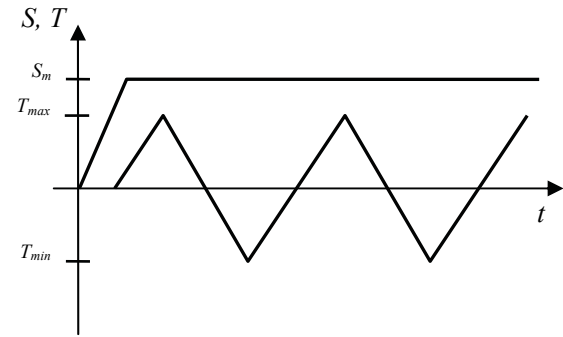


Figure 4: Schematic representation of a constant tensile and a cyclic torsional loading component

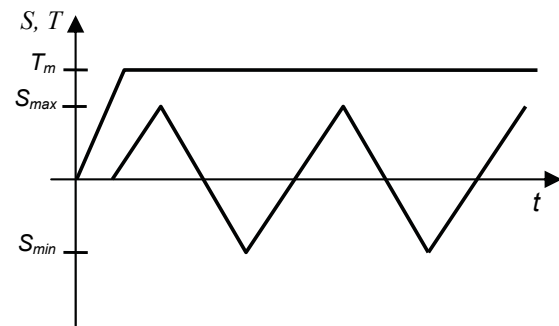


Figure 5: Schematic representation of a cyclic tensile and a constant torsional loading component

shear stress amplitude  $T_a$  is used to describe the loading combination. The values of  $S_m$  and  $T_a$  are chosen in such a way that a wide range of  $c$ -values ( $c=0$  to  $c=10$ ) can be covered, whereas the nominal equivalent stress  $S_{eq}$  is kept constant and larger than the value of the material's yield stress  $\sigma_y$ .

At the beginning of the loading, the tensile component in loading cases L1 to L6 increases linearly with increasing time, while the torsional component is kept to be zero. After reaching the maximum value of the tensile loading component, the cyclic torsional loading component takes its action (see Fig. 4).

##### 4.2 Loading group 2: Constant torsion combined with cyclic tension

Four combinations (loading cases L7 to L10) of constant torsion and cyclic fully reversed tension-compression with constant amplitudes ( $R_{\sigma} =$

Table 2: Constant tension - cyclic torsion loading cases

No	$c$	$S_m$ N/mm <sup>2</sup>	$T_a$ N/mm <sup>2</sup>	$R_\tau$	$S_{eq}$ N/mm <sup>2</sup>
L1	0	0	225.63	-1	390.8
L2	0.623	132.26	212.31	-1	390.8
L3	1.000	195.40	195.40	-1	390.8
L4	1.605	265.62	165.49	-1	390.8
L5	5.000	369.27	73.85	-1	390.8
L6	10.00	385.07	38.50	-1	390.8

$S_{min}/S_{max} = -1$ ) are investigated. A schematic representation of this loading type is shown in Fig. 5, while the details of the loading components are summarized in Tab. 3.

Here, the ratio  $d = T_m/S_a$  of the constant nominal shear stress  $T_m$  and the nominal normal stress amplitude  $S_a$  is introduced as a characteristic loading parameter. The values of  $T_m$  and  $S_a$  are chosen in such a way that the range of  $d = 0$  to  $d = 10$  is covered, while the nominal equivalent stress  $S_{eq}$  is taken to be constant.

At the beginning of loading cases L7 to L10, the torsional component increases linearly with increasing time, while the tensile component is kept to be zero. After the torsional loading component reached its maximum value, the cyclic tensile loading component starts with its action.

It should be mentioned that severe tensile and torsional loading cases are investigated, resulting in excessive plastic strain values especially at the notch-root. However, some of the loading levels are taken intentionally extremely high (compared to the real in-service loading situations) in order to clearly reveal the multiaxial plastic material behavior and to gain more reliable conclusions.

## 5 Numerical results and discussion

The obtained numerical results are presented as normal stress-normal strain and shear stress-shear strain diagrams at the failure-critical notch-root. For clarity of the presentation, each loading case is specified by an abbreviated notation like F20-L4. Here, the first letter refers to the mesh type ("F" for a fine FE mesh and "C" for a coarse mesh). If no mid-nodes in the used elements are introduced in the numerical calculations, then a

letter "N" follows. The following number (e.g. 20, 5 or 3) refers to the number of segments used in the multilinear approximation (e.g. 20 for 20-segments, 5 for 5-segments or 3 for 3-segments approximation of the nonlinear stress-strain curve, respectively). The last part of the abbreviated notation refers to the loading case as described in the last section (e.g., L1 to L10).

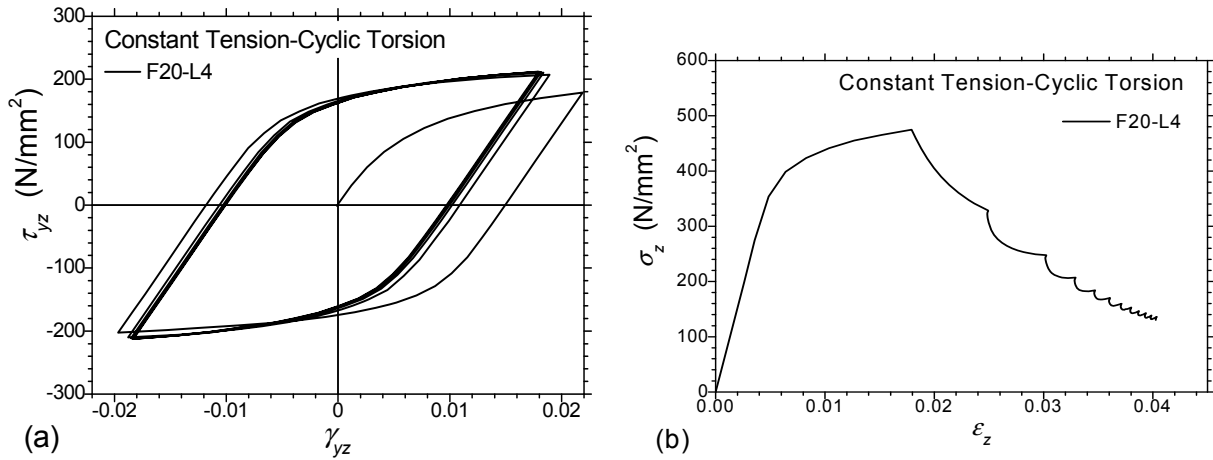
### 5.1 Local stress-strain relations at the notch-root

#### 5.1.1 Loading group 1: Constant tension combined with cyclic torsion

As a representative example for the loading combination consisting of a constant tension and a cyclic torsion, the stress-strain relations at the notch-root are presented in Fig. 6 for the loading case L4. A fine FE mesh and 20-segments for the nonlinear elastic-plastic stress-strain curve of the material are applied in the numerical calculations. Fig. 6a represents a typical cyclic  $\tau_{yz} - \gamma_{yz}$ -path for cyclic torsion superimposed by constant tension. The shear stress-strain curve shows a kind of "structural" hardening behavior. It should be remarked here that this "structural" hardening phenomenon differs from the well known cyclic hardening or ratcheting behavior that occurs under general non-proportional loading conditions and which cannot be described by the multilayer model of Besseling. A comprehensive discussion and further references dealing with the capability and the failure of Besseling's model to describe the cyclic hardening behavior have been given by Rother (2005). The stabilized hysteresis of the cyclic shear stress-strain curve is established after a few loading cycles. In addition, the stabilized hysteresis obeys the so-called Masing behavior,

Table 3: Monotonic torsion - cyclic tension-compression loading cases

No	$d$	$T_m$ N/mm <sup>2</sup>	$S_a$ N/mm <sup>2</sup>	$R_\sigma$	$S_{eq}$ N/mm <sup>2</sup>
L7	0	0	390.80	-1	390.8
L8	0.623	65.49	265.63	-1	390.8
L9	1.000	195.40	195.40	-1	390.8
L10	10.00	225.25	22.52	-1	390.8

Figure 6: Stabilization procedures of (a) the  $\tau_{yz} - \gamma_{yz}$  path and (b) the  $\sigma_z - \varepsilon_z$  path corresponding to load case L4

see Masing (1926).

The corresponding  $\sigma_z - \varepsilon_z$ -path presented in Fig. 6b shows a typical elastic-plastic material behavior corresponding to the material law as long as the tensile loading component is acting alone. After the onset of the torsional loading component, the  $\sigma_z - \varepsilon_z$  curve depicts a diminishing behavior, i.e. the local stress  $\sigma_z$  decreases with increasing strain  $\varepsilon_z$ . The decrease of the stress component  $\sigma_z$  is a consequence of the applied von Mises yield criterion. Since the equivalent yield stress for a given material remains constant independent of the uniaxial or the multiaxial stress state, the  $\sigma_z$ -component has to be decreased in the presence of an additional shear stress component  $\tau_{yz}$ .

Since stabilized cyclic shear stress-strain curves can be obtained after few loading cycles, they are the most important part for the evolution of fatigue damage and the prediction of the fatigue life of notched structures. The influences of the ratio  $c = S_m/T_a$  on the stabilized local shear stress-strain curves at the notch-root are shown in Fig. 7. Here it can be recognized that the magnitude

of the ratio  $c$  affects directly the extension of the cyclic plastic deformation. The  $\tau_{yz} - \gamma_{yz}$ -curves presented in Fig. 7 show that a gradual increase of the loading parameter  $c$  (from L1 to L6) results in a reduction of the stabilized shear stress-shear strain hysteresis loop.

### 5.1.2 Loading group 2: Constant torsion combined with cyclic tension

As a representative example for the loading combination of a constant torsion and a cyclic tension, Fig. 8 shows the stress-strain curves at the notch-root for the loading case L8. Also here, a fine FE mesh and 20-segments for approximating the nonlinear elastic-plastic stress-strain curve of the material are used in the numerical calculations.

Figure 8a shows a typical cyclic  $\sigma_z - \varepsilon_z$ -curve for constant torsion and cyclic tension. It exhibits a structural hardening behavior. The stabilized hysteresis of the cyclic normal stress-normal strain curve is established after a few loading cycles. The stabilized hysteresis obeys the Masing behavior.

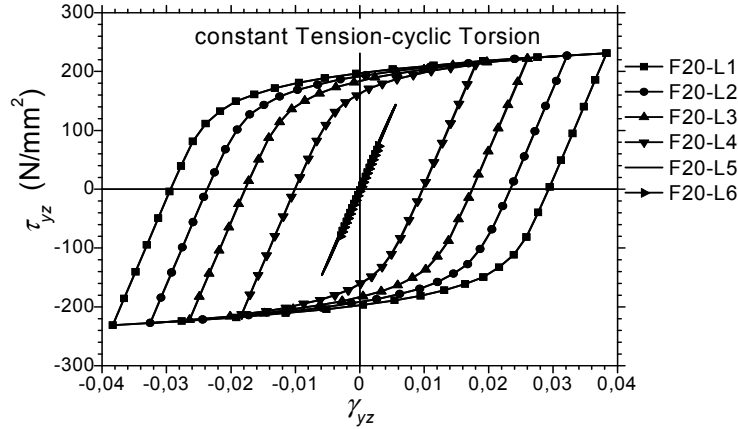


Figure 7: Influence of the c-parameter on the formation of the hysteresis loops for the load cases L1 to L6

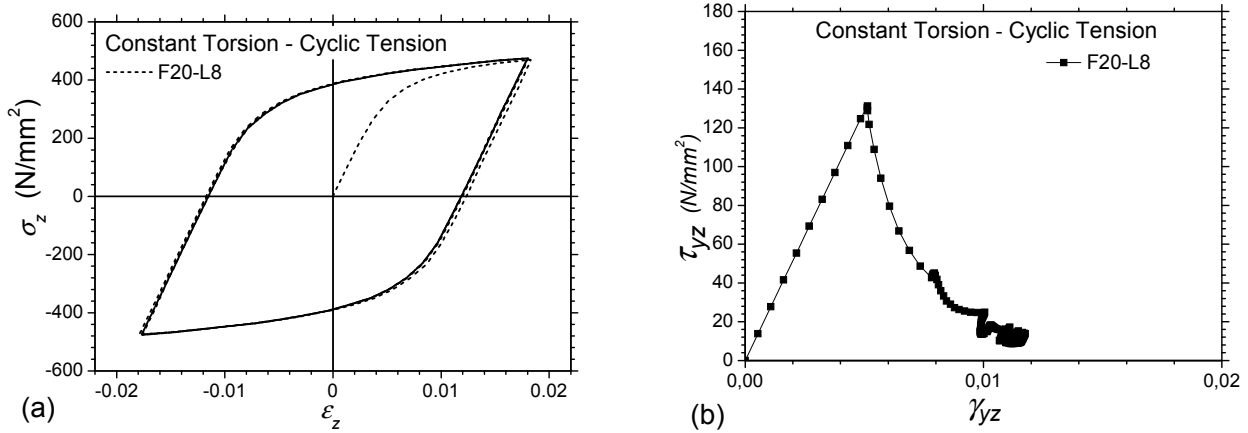


Figure 8: Stabilized (a)  $\sigma_z - \epsilon_z$  - curve and (b)  $\tau_{yz} - \gamma_{yz}$  - curve for load case L8

The corresponding  $\tau_{yz} - \gamma_{yz}$ -path is presented in Fig. 8b, which shows an elastic-plastic material behavior corresponding to the material law when the torsional loading component is acting alone. After the onset of the tensile loading component, the  $\tau_{yz} - \gamma_{yz}$ -curve depicts a softening behavior, i.e. the local shear stress  $\tau_{yz}$  decreases with increasing shear strain  $\gamma_{yz}$ .

Similar to Fig. 7 for constant tension and cyclic torsion, a gradual increase of the loading parameter  $d = T_m/S_a$  causes a reduction in the extent of the stabilized normal stress-normal strain hysteresis loop, as can be seen in Fig. 9.

### 5.2 Effect of the FE meshes

To investigate the effects of the used FE-meshes on the numerical results for the normal stress-

normal strain and shear stress-shear strain curves at the notch-root, two different meshes with a coarse and a fine meshing near the notch-root are investigated, and the results are presented and discussed in the following. In addition, the influence of the introduction of mid-nodes is also investigated in conjunction with the fine mesh.

In Fig. 10, the  $\sigma_z - \epsilon_z$ -curves corresponding to the load case L6, for the fine mesh (F) and the coarse mesh (C) are presented. In addition, the numerical results for the same load case but without mid-nodes (N) in the finite elements are also given in Fig. 10. All results are obtained using 20 segments for approximating the material's stress-strain curve.

Fig. 10 shows that the mesh refinement has a considerable effect on the computed local stress  $\sigma_z$

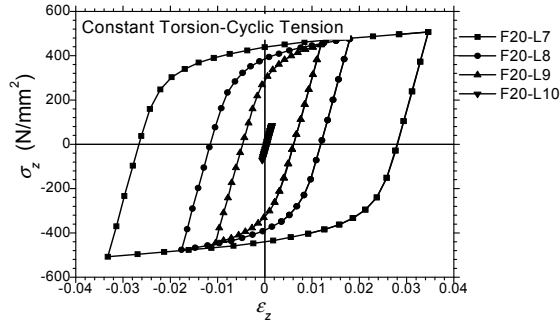


Figure 9: Influence of the d-parameter on the formation of the hysteresis loops for the load cases L7 to L10

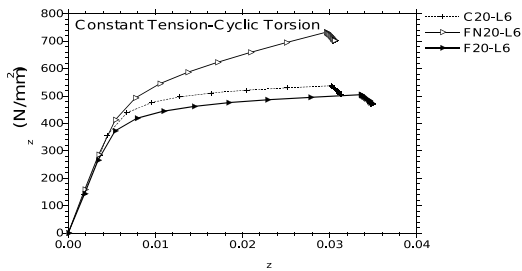


Figure 10: Influence of mesh refinement and mid-node application on the  $\sigma_z - \epsilon_z$  - curve for the load case L6

and local strain  $\epsilon_z$  at the notch-root. The use of the coarse mesh as presented here causes a radial stress component  $\sigma_r$  at the notch-root element, where no radial stress should appear theoretically. This is, however, a pure numerical effect caused by the stress extrapolation from the interior Gaussian points to the element nodes. The influence of this pure numerical effect on the local  $\sigma_z - \epsilon_z$ -path increases with increasing loading amplitude and consequently the plastic deformations.

An increase of the integration points for a fixed number of elements can lead to a significant reduction of the stress component  $\sigma_r$ . On the other hand, for a fixed number of integration points, an increase of the element number can also reduce the stress component  $\sigma_r$ . Since the material yields at the same equivalent stress value, the reduction of  $\sigma_r$  leads to a smaller  $\sigma_z$ -value as shown in Fig. 10 comparing the curves resulting from the coarse

and the fine FE meshes.

To clarify the abovementioned effect, the stress values obtained by using the coarse and the fine FE meshes for the simple case of a pure static tensile loading of the notched cylinder with a nominal tensile stress  $S=233$  MPa are presented in Tab. 4. For this loading case, plastic strain occurs at the notch-root.

Fig. 11 presents the distribution of the stress component  $\sigma_r$  computed at the net section element-nodes for a pure tension.

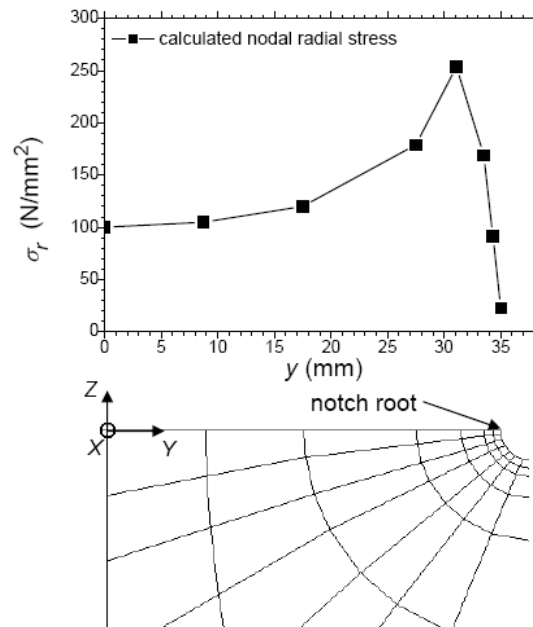


Figure 11: Distribution of the calculated  $\sigma_r$  values along the y-axis of the net section of the shaft

Similar qualitative findings are reported by Jiang (2004). Since the  $\sigma_r$ -distribution in the radial direction possesses a large gradient from the axis of symmetry to the notch-root, as shown in Fig. 11, the extrapolation of the stress values from the interior Gaussian points to the surface nodes on the notch-root results in the presence of an erroneous  $\sigma_r$  component. With increasing element size on the shaft surface at the notch-root the extrapolation error in the computation of the  $\sigma_r$ -value increases. A significant reduction of the extrapolation error in computing the radial stress component  $\sigma_r$  at the notch-root can be obtained by im-

Table 4: Influence of mesh refinement on the radial stress percentage relative to the axial stress

	$\sigma_z(\text{N/mm}^2)$	$\sigma_r(\text{N/mm}^2)$	$\sigma_r/\sigma_z$	$\sigma_r$ (%)
Fine mesh	463.3	21.63	21.4	4.6
Coarse mesh	496.3	64.67	7.67	13

proving the meshing quality near the notch-root.

The influence of the element mid-nodes on the numerical results can be quantified by comparing the corresponding results obtained by the fine mesh with and without mid-nodes as presented in Fig. 10. Remarkable deviations between the corresponding curves can be observed even at small plastic deformations. The deviations increase with increasing plastic deformations.

Figure 12 shows the stabilized  $\sigma_z - \varepsilon_z$ -hystereses for the loading cases L7 and L8 determined by means of the coarse mesh including mid-nodes and the fine mesh with and without mid-nodes.

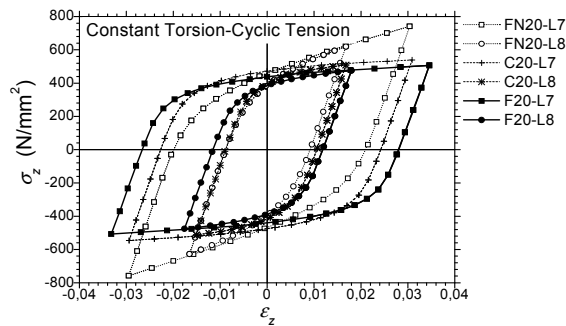


Figure 12: Influence of mesh refinement and mid-node application on the  $\sigma_z - \varepsilon_z$  state for load cases L7 and L8

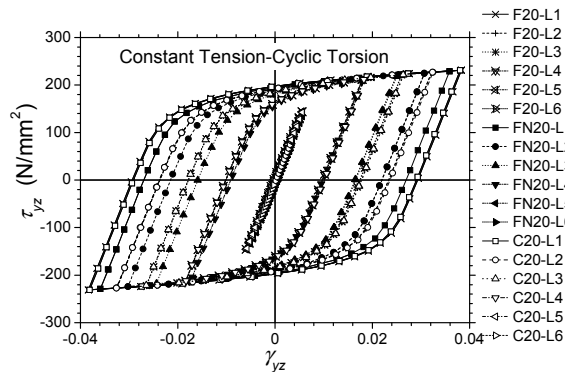


Figure 13: Influence of mesh refinement and mid-node application on the  $\tau_{yz} - \gamma_{yz}$  state for the load cases L1 to L6

Here, a constant torsional load acts simultaneously with a cyclic tensile load component. The stabilized  $\sigma_z - \varepsilon_z$ -hystereses determined by the coarse mesh show smaller plastic deformations and higher stresses compared to the ones determined by the fine mesh. This is apparent for the loading cases L7 and L8, where notable plastic deformations arise.

Similar to the results for the loading group “constant tension + cyclic torsion”, the differences between the results obtained by a coarse mesh and a fine mesh are mainly due to a numerically erroneous  $\sigma_r$ -component at the notch-root. Since  $\sigma_r$  and  $\sigma_z$  have the same sign,  $\sigma_r$  suppresses the axial deformation, although  $\sigma_r$  does not produce any radial plastic deformation at the notch-root due to its low value. Accordingly, the material at the notch-root in the model with a coarse mesh behaves stiffer than in reality. With increasing element number the value of the erroneous  $\sigma_r$ -component decreases and its influence on the  $\sigma_z - \varepsilon_z$  response becomes negligible. Here again, when finite elements without mid-nodes are applied, the calculated  $\sigma_r$ -values become remarkable and may influence the  $\sigma_z - \varepsilon_z$ -hysteresis significantly. As shown in Fig. 12, the  $\sigma_z - \varepsilon_z$ -curves obtained using elements without mid-nodes possess stiffer slopes, lower plastic deformations and higher stresses compared to the ones with mid-nodes. The results given in Figs. 10 and 12 point out the significance of a fine meshing in the notch-root area and the contribution of the element mid-nodes to achieve accurate numerical results, especially when large plastic deformations arise at the notch-root.

Figure 13 shows the stabilized  $\tau_{yz} - \gamma_{yz}$ -hystereses at the notch-root for the loading cases L1 to L6 (constant tension + cyclic torsion) determined by means of various mesh types.

It can be observed that there are no significant influences of the coarse and fine meshes with mid-

nodes on the computed results. In the loading cases L4, L5 and L6, the influence of the mid-nodes on the numerical results is negligible. Contrary to the notable contribution of the element mid-nodes to the evaluated  $\sigma_z - \varepsilon_z$ -curves at the notch-root, which is mainly caused by the numerically erroneous radial stress component  $\sigma_r$ , the  $\tau_{yz} - \gamma_{yz}$ -curves are not significantly affected by the mesh refinement and the application of the element mid-nodes, as can be concluded from the numerical results shown in Fig. 13. This is due to the smaller shear stress gradient and the larger normal stress gradient in the notch-root area. To confirm this fact, the distribution of the gradient of the stress concentration factor under pure tension ( $S=80$  MPa) and pure torsion ( $T=40$  MPa) along the notch-surface profile is shown in Fig. 14.

### 5.3 Influences of the segment number for the stress-strain curve approximation

The influences of the segment number used for the approximation of the stress-strain curve on the computed stresses and strains at the notch-root are investigated for three different segment numbers, namely 3, 5 and 20 segments. The load cases L1 to L10 given in Tab. 2 and 3 are considered.

Figure 15 shows the stabilized  $\tau_{yz} - \gamma_{yz}$ -curve obtained from the coarse FE mesh with mid-nodes for the load cases L9 and L10.

Significant deviations between the numerical results from the 3 segments and the 5 segments approximations can be observed. However, the deviations of the numerical results determined by the 5 and the 20 segments approximations are of less significance.

The corresponding  $\sigma_z - \varepsilon_z$ -hystereses for the load cases L7, L9 and L10 are plotted in Fig. 16.

Noticeable discrepancies between the numerical results obtained by the 3 and the 5 segments approximations are observed. On the other hand, satisfactory agreement between the hystereses determined with the 5 and the 20 segments approximations are obtained.

Similar conclusions can also be drawn for load cases consisting of constant tensile and cyclic tor-

sional components. Figures 17 and 18 show some selected  $\sigma_z - \varepsilon_z$ -curves and stabilized  $\tau_{yz} - \gamma_{yz}$ -hystereses, respectively. Here the numerical results show again that the discrepancies between the 5 and the 20 segments approximations are negligible, contrary to the notable discrepancies between the 3 and the 5 segments approximations.

In general, the 3 segments approximation provides numerical results with a higher plastic deformation in all loading cases considered, whereas the differences in the computed stresses are not significant. According to the present study, stress-strain curve approximations with 5 to 20 segments are sufficient to yield qualitatively and quantitatively satisfactory results.

An additional factor that should be taken into account is the computational effort of the different stress-strain curve approximations, especially in engineering applications with more complex geometries than the one investigated here. Tab. 5 contains the required computing times for the notched cylinder as percentages of the “most reliable” computation, i.e. the use of a fine mesh including mid-nodes together with a 20 segments approximation. For comparison purposes, the computing time needed by the bilinear kinematic hardening rule is also incorporated in Tab. 5.

It can be concluded from Tab. 5 that the computing time without mid-nodes can be reduced to approximately 1/3 of the time required by the “most reliable” computation. In combination with a coarse mesh, the computing time reduction may reach even 21% of that of the “most reliable” computation. This significant saving in computing time may be of practical interest especially when pure torsional load components affect the stress-strain response at the failure-critical locations of an engineering component. On the other hand, the used segment number to approximate the material’s stress-strain curve does not have a worth-mentioning influence on the computing time.

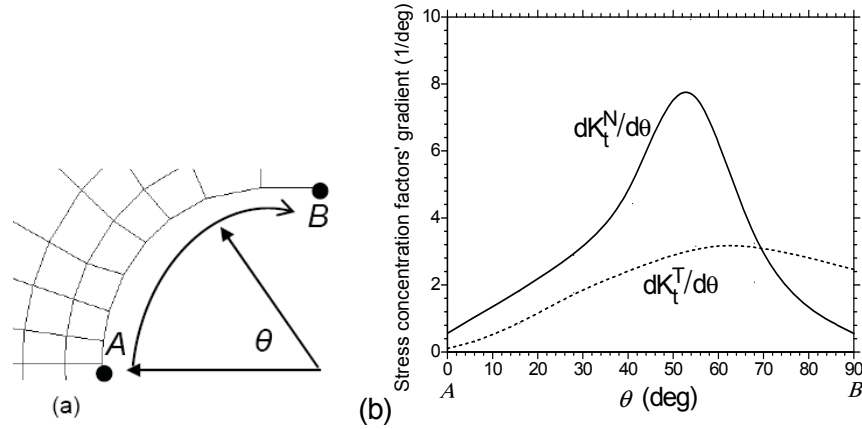


Figure 14: (a) Fine mesh detail including mid-nodes, and (b) distributions of the  $K_t^S$  and  $K_t^T$  gradients along the notch surface under pure tension and pure torsion, respectively

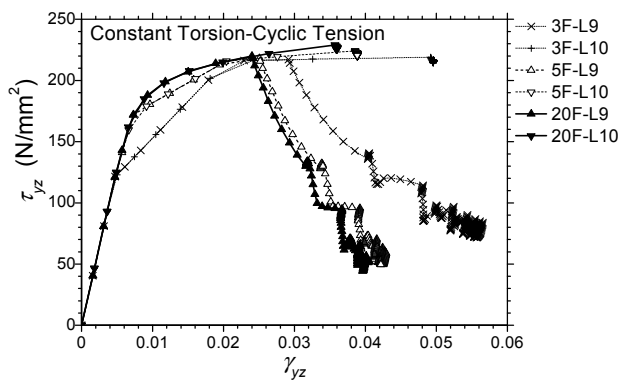


Figure 15: Influence of the number of segments for the approximation of the material law on the  $\tau_{yz} - \gamma_{yz}$  state for the load cases L9 and L10

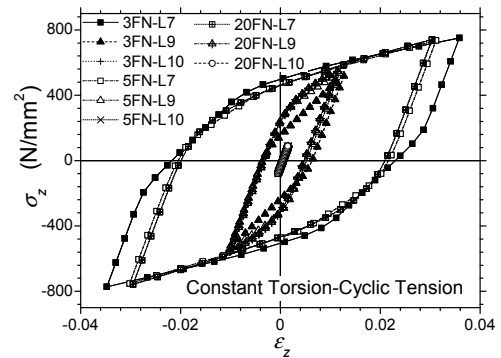


Figure 16: Influence of the number of segments for the approximation of the material law on the  $\sigma_z - \epsilon_z$  state for the load cases L7, L9 and L10

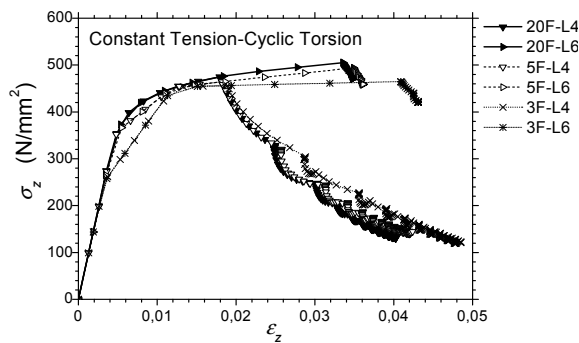


Figure 17: Influence of the number of segments for the approximation of the material law on the  $\sigma_z - \epsilon_z$  state for the load cases L4 and L6

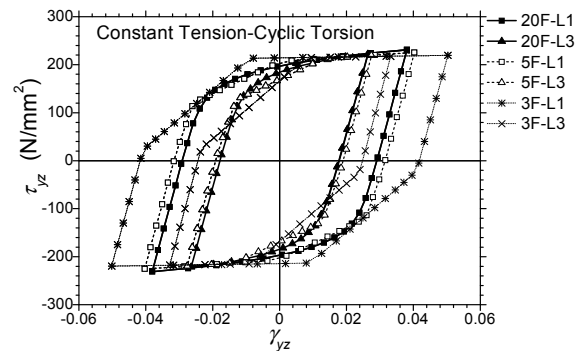


Figure 18: Influence of the number of segments for the approximation of the material law on the  $\tau_{yz} - \gamma_{yz}$  state for the load cases L1 and L3

#### 5.4 Comparison of the numerical results from the bilinear and the multilinear approximations

To compare the numerical results obtained by the bilinear and the multilinear approximations,

two representative examples are considered here. In the first example, a pure cyclic tension-compression corresponding to the loading case L7

Table 5: Relative computing time in (%) dependent on the number of finite elements and segments applied for the approximation of the material law

Number of segments	Mid nodes applied				Without mid nodes			
	20	5	3	2	20	5	3	2
Fine mesh	100	95	91	89	35	32	30	29
Coarse mesh	75	71	68	66	26	23	21	20

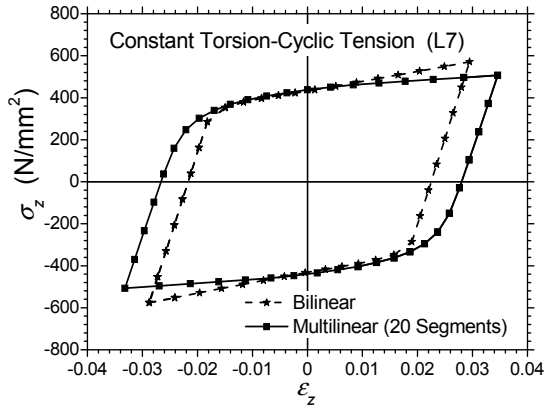


Figure 19: Comparison of stress-strain hystereses determined from the bilinear and the multilinear material law approximations for the load case L7

is investigated. The stabilized stress-strain hystereses at the notch-root of the cylinder, provided by the bilinear Prager-Ziegler kinematic hardening rule and the multilayer model of Besseling, are presented in Fig. 19. In the application of the multilayer model of Besseling, a multilinear approximation of the cyclic stress-strain curve of Al5083 is used.

Even in this simple case of uniaxial tension-compression, where no shear stress affects the stress-strain state at the notch-root, considerable deviations in the normal stress-normal strain relation can be recognized. The bilinear approximation gives rise to a larger peak stress, while the multilinear approximation yields a larger peak strain.

In the second example, a constant tension superimposed by a cyclic torsion corresponding to the loading case L2 is investigated. The normal stress-normal strain paths obtained by the bilinear and the multilinear approximations are shown in Fig. 20. Here again, the bilinear approximation

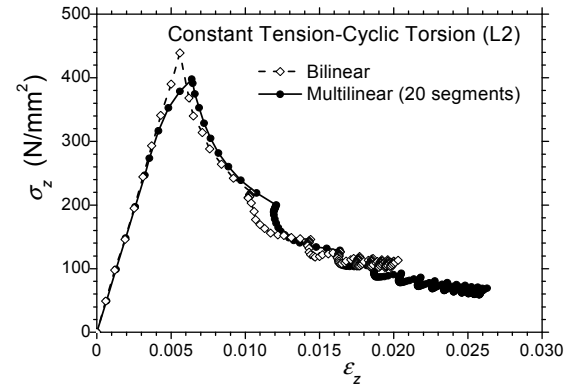


Figure 20: Comparison of  $\sigma_z - \varepsilon_z$  paths determined from the bilinear and the multilinear material law approximations for the load case L2

leads to a higher peak stress, while the multilinear approximation yields a larger plastic strain at the notch-root. This implies that the bilinear approximation gives rise to a stiffer material response at the notch-root than the multilinear one.

## 6 Conclusions

This paper presents an elastic-plastic FE analysis of a circumferentially notched cylinder subjected to synchronous non-proportional multiaxial fatigue loading consisting of constant and cyclic loading components. The multilayer or overlay model of Besseling in conjunction with the von Mises yield criterion is applied to describe the elastic-plastic material behavior. The following conclusions can be drawn:

- The stabilized hysteresis resulting from the cyclic loading component is established after few loading cycles and shows the Masing behavior.
- The stress-strain path resulting from the con-

stant loading component possesses a softening effect.

- The quality of the FE mesh affects the accuracy of the numerical results for the local stresses and strains at the notch-root. The use of a fine mesh with mid-nodes provides a satisfactory description of the stress-strain state in the notch-root area. Although the computing time required by a FE mesh with mid-nodes may increase up to three times of the time using the same mesh without mid-nodes, it is necessary to use mid-nodes in order to achieve sufficiently accurate stress and strain results, especially when normal stresses and/or large plastic deformations arise at the notch-root. The influence of the mesh quality on the computed stresses and strains at the notch-root is of less significance for a mild notch as investigated here. However, it is expected that the influence of the mesh refinement on the computed stresses and strains for sharper notches with more pronounced stress concentrations may become crucial which needs further investigations.
- The segment-number used to approximate the elastic-plastic stress-strain curve of the material has a substantial influence on the numerical results of the local stresses and strains at the notch-root. The present analysis confirms that five or more segments are adequate to accurately compute the local stress-strain responses at the notch-root. The increase in the computing time by using 5 to 20 segments and a fine mesh with mid-nodes remains below 10% of the time using an unsatisfactory 3 segments approximation.
- The multilayer model of Besseling yields a larger plastic strain, while the bilinear kinematic hardening rule of Prager and Ziegler results in a larger peak stress. It is expected that the multilayer model of Besseling is more adequate to describe the nonlinear elastic-plastic material behavior in general cases.

**Acknowledgement:** Support by the State Scholarships Foundation of Greece (IKY) and the German Academic Exchange Service (DAAD) is gratefully acknowledged.

## References

- ANSYS, Inc.** (2007): Theory Reference, Chapter 4. Structures with material nonlinearities, special-ization for multilinear kinematic hardening.
- Bathe, K.** (1996): Finite Element Procedures. Prentice Hall, New Jersey.
- Besseling, J.F.** (1958): A theory of elastic, plastic, and creep deformations of an initially isotropic material showing anisotropic strain-hardening creep recovery and secondary creep. *ASME J Appl Mech*, vol. 25, pp. 529-536.
- Chiang, D.Y.; Beck, J.L.** (1994): A new class of distributed-element models for cyclic plasticity – I. Theory and application. *Int J Solids Structures*, vol. 31, pp. 469-484.
- Chiang, D.Y.; Beck, J.L.** (1994): A new class of distributed-element models for cyclic plasticity – II. On important properties of material behavior. *Int J Solids Structures*, vol. 31, pp. 485-496.
- Döring, R.; Hoffmeyer, J.; Seeger, T.; Vormwald, M.** (2003): A plasticity model for calculating stress strain sequences under Multi-axial non-proportional cyclic loading. *Computational Materials Science*, vol. 28, pp.587-596.
- Hasan, T.; Kiriakides, S.** (1994): Ratcheting of cyclically hardening and softening materials II. Multiaxial behaviour. *Int. J Plasticity*, vol. 10, No2, pp. 149-184.
- Hertel, O.; Döring, R.; Hoffmeyer, J.; Seeger, T.; Vormwald, M.** (2005): Notch stress and strain approximation procedures for application with multiaxial nonproportional loading, *MP Materials Testing*, vol. 47, pp. 268-277.
- Hoffmann, M.; Seeger, T.** (1985): A generalized method for estimating multiaxial elastic-plastic notch stresses and strains. *ASME J Engng Mater Tech*, vol. 107, pp. 250-254.
- Iwan, W.D.** (1966): A distributed element model for hysteresis and its steady-state dynamic response. *ASME J Appl Mech*, vol. 33, pp. 893-

900.

**Iwan, W.D.** (1967): On a class of models for the yielding behaviour of continuous and composite systems. *ASME J Appl Mech*, vol. 34, pp. 612-617.

**Jiang, Y.** (2001): Deformation analysis of notched components and assessment of approximate methods. *Fat Fract Eng Mat Struct*, vol. 24, pp. 729-740.

**Köttgen, V. B.; Seeger, T.** (1993): A Mas- ing type integration of the Mroz model for some non-proportional stress-controlled paths. Heft FF-6/1993, Institut für Stahlbau und Werkstoffmechanik der TH Darmstadt.

**Lemaitre, J.; Chaboche, J.L.** (1990): *Mechanics of Solid Materials*, Cambridge University Press.

**Masing, G.** (1926): Eigenspannungen und Verfestigung beim Messing. In: *2<sup>nd</sup> Int Congress Appl Mech*, pp. 332-335.

**Mroz, Z.** (1967): On the description of anisotropic work hardening. *J Mech Phys Solids*, vol. 17, pp. 163-175.

**Owen, D.R.; Prakash, A.; Zienkiewicz, O.C.** (1974): Finite element analysis of non-linear composite materials by use of overlay systems. *Computers & Structures*, vol. 4, pp. 1251-1267.

**Peterson, R.E.** (1974): *Stress Concentration Factors*, John Wiley & Sons, New York.

**Prager, W.** (1955): The theory of plasticity: A survey of recent achievements In: *Proc. Inst. Mech. Engrs.*, vo. 169, pp. 41-57.

**Pande, G.N.; Owen, D.R.J.; Zienkiewicz, O.C.** (1977): Overlay models in time-dependent non-linear material analysis. *Computers & Structures*, vol. 7, pp. 435-443.

**Ramberg, W.; Osgood, W.R.** (1943): Description of stress-strain curves by three parameters. NACA Technical Note No. 902.

**Rother, K.** (2005): Beitrag zur rechnerischen Lebensdaueranalyse bei mehrachsiger, nichtproportionaler Beanspruchung. Heft 76, Institut für Stahlbau und Werkstoffmechanik der TU Darmstadt.

**Savaidis, A.** (1994): Finite-Element Untersuchungen und Entwicklung eines Näherungsver-

fahrens zur Beschreibung mehrachsiger elastisch-plastischer Kerbbeanspruchungen bei nichtproportionaler zyklischer Belastung. *Stahlbau und Werkstoffmechanik der TU Darmstadt*, vol. 52, Germany.

**Savaidis, G.** (1995): Berechnung der Bauteilanrisslebensdauer bei mehrachsigen proportionalen Beanspruchungen. Heft 54, Institut für Stahlbau und Werkstoffmechanik der TH Darmstadt.

**Savaidis, A; Savaidis, G.; Zhang, Ch.** (2001): FE fatigue analysis of notched elastic-plastic shaft under multiaxial loading consisting of constant and cyclic components. *Int J Fatigue*, vol. 23, pp. 303-315.

**Savaidis, A; Savaidis, G.; Zhang, Ch.** (2001): Elastic-plastic FE analysis of a notched shaft under multiaxial nonproportional cyclic loading. *Theor Appl Fract Mech*, vol. 32, pp. 87-97.

**Savaidis, A; Savaidis, G.; Zhang, Ch.** (2002): Numerical analysis of notched elastic-plastic structures under multiaxial variable amplitude loading. *Computers & Structures*, vol. 80, pp.1907-1918.

**Schiffner, K.** (1995): Overlay models for structural analysis under cyclic loading. *Computers & Structures*, vol. 56, pp. 321-328.

**von Mises, R.** (1913): Mechanik der festen Körper im plastisch-deformablen Zustand. In: *Nachr. Konigl. Ges. Wiss. Göttingen, Math. Phys. Kl.*, pp. 582-593.

**Yoon, S.; Hong, S.G.; Lee, S.B.** (2004): Phenomenological description of cyclic deformation using the overlay model. *Mater Sci Eng, A* 364, pp. 17-26.

**Ziegler, H.** (1959): A modification of Prager's hardening rule. *Quart. Appl. Math.*, vol. 17, pp. 55-60.